

# Post-deposition Activation of Latent Hydrogen-Bonding: A New Paradigm for Enhancing the Performances of Bulk Heterojunction Solar Cells

Francesco Bruni, Mauro Sassi, Marcello Campione, Umberto Giovanella, Riccardo Ruffo, Silvia Luzzati, Francesco Meinardi, Luca Beverina,\* and Sergio Brovelli\*

Small conjugated molecules (SM) are gaining momentum as an alternative to semiconducting polymers for the production of solution-processed bulk heterojunction (BHJ) solar cells. The major issue with SM-BHJs is the low carrier mobility due to the scarce control on the phase-segregation process and consequent lack of preferential percolative pathways for electrons and holes to the extraction electrodes. Here, a new paradigm for fine tuning the phase-segregation in SM-BHJs, based on the post-deposition exploitation of latent hydrogen bonding in binary mixtures of PCBM with suitably functionalized electron donor molecules, is demonstrated. The strategy consists in the chemical protection of the H-bond forming sites of the donor species with a thermo-labile functionality whose controlled thermal cleavage leads to the formation of stable, crystalline, phase-separated molecular aggregates. This approach allows the fine tuning of the nanoscale film connectivity and thereby to simultaneously optimize the generation of geminate carriers at the donor–acceptor interfaces and the extraction of free charges via ordered phase-separated domains. As a result, the PV efficiency undergoes an over twenty-fold increase with respect to control devices. This strategy, demonstrated here with mixtures of diketopyrrolopyrrole derivatives with PCBM can be extended to other molecular systems for achieving highly efficient SM-BHJ solar cells.

## 1. Introduction

Over the last two decades, bulk-heterojunction solar cells based on binary mixtures of polymeric p-type electron donors and n-type fullerene acceptors<sup>[1]</sup> have received enormous interest from both the academic community and the industry as promising candidates for replacing silicon in photovoltaic (PV) devices fabricated through cost-effective solution-based methods on flexible or bendable substrates.<sup>[2]</sup> Advancements in terms of morphological control and manipulation,<sup>[3]</sup> fundamental understanding of their photophysical<sup>[4]</sup> and transport properties<sup>[5]</sup> as well as device architecture<sup>[6,7]</sup> have allowed to reach efficiencies up to 9%.<sup>[8,9]</sup> However, solar cells based on polymeric systems still suffer of intrinsic limitations that hinder their scale up to mass production. Specifically, chain length polydispersity, structural defects and contamination with polymerization precursors, byproducts and metal based catalysts result in limited batch-to-batch reproducibility and poor control over the device perfor-

mances.<sup>[10]</sup> For these reasons, increasing attention is recently being diverted to so-called “small molecule” bulk-heterojunction (SM-BHJ) solar cells where the long-chain polymer donors are replaced with conjugated molecular systems that can be synthesized with well defined molecular structure tuned to match the light harvesting capabilities and oxidation potential/electron affinity of the best performing polymeric materials.<sup>[11]</sup> In only a few years, SM-BHJ solar cells have held their promise and reached efficiencies up to over 10%.<sup>[12]</sup> Recently, Mitsubishi Chemical announced world record efficiency of 11.7% using a binary mixture of benzoporphyrins and fullerene derivatives.<sup>[13]</sup>

With respect to traditional silicon solar cells where free charges are generated directly upon photoexcitation, splitting of excitons in organic semiconductors requires to overcome a larger potential barrier (exciton binding energy >50 meV)<sup>[14]</sup> owing to the lower dielectric constant of the medium. In BHJ solar cells, this is typically achieved by mixing materials with different electron affinity and oxidation potential, so as to form

F. Bruni, Dr. M. Sassi, Prof. R. Ruffo,  
Prof. F. Meinardi,  
Prof. L. Beverina, Prof. S. Brovelli  
Dipartimento di Scienza dei Materiali  
Università degli Studi di Milano-Bicocca  
via Cozzi 55, 20125, Milano, Italy  
E-mail: luca.beverina@unimib.it;  
sergio.brovelli@unimib.it

Prof. M. Campione  
Dipartimento di Scienze dell'Ambiente e del Territorio e di  
Scienze della Terra  
Università degli Studi di Milano-Bicocca  
Piazza della Scienza 1, 20126, Milano, Italy  
Dr. U. Giovanella, Dr. S. Luzzati  
Istituto per lo Studio delle Macromolecole  
Consiglio Nazionale delle Ricerche  
(ISMMac-CNR)  
Via Bassini 15, 20133, Milano, Italy



DOI: 10.1002/adfm.201400896

distributed interfaces where excitons are split in geminate electron-hole pairs by ultrafast charge transfer processes.<sup>[15]</sup> Because of the typical homopolar conductivity of organic materials, the transport of electrons and holes to the respective electrodes requires preferential percolation pathways of p- and n-type character that are formed by separating the donor and the acceptor moieties in phase segregated domains. In order to optimize the photovoltaic efficiency it is therefore pivotal to finely balance the degree of mixing: on the one hand, a fine interpenetration assures that the size of segregated domains does not exceed the exciton diffusion length, which would suppress exciton splitting into geminate e-h pairs at the donor/acceptor interface; on the other hand, phase separation into highly conductive crystalline domains promotes efficient long-range geminate charge separation and transport.<sup>[16,17]</sup> In addition, molecular orientation<sup>[18]</sup> and interdiffusion of molecular species between phase separated domains have been recently shown to significantly affect the performances of BHJ solar cells,<sup>[19]</sup> thereby further highlighting the relevance of developing means to fine tune the self-assembly and segregation processes in molecular blends.

In polymer-fullerene blends, phase segregation happens spontaneously due to their unfavorable entropy of mixing, yielding highly interpenetrated phase separated domains (10–20 nm in size)<sup>[20]</sup> whose extent can be further controlled through post processing techniques, such as thermal or solvent vapor annealing.<sup>[21]</sup> In contrast, phase separation in SM-BHJs lacks of entropic contribution and therefore requires an additional driving force to occur. In order to address this issue, several groups have adopted various approaches including the exploitation of different solubility of the blend constituents in the processing solvents,<sup>[22]</sup> the insertion of additives<sup>[23]</sup> and the adoption of post-processing procedures such as solvent vapor and/or thermal annealing.<sup>[24]</sup> Phase segregation can be further promoted by increasing the dipolar character of the donor species or by exploiting  $\pi$ - $\pi$  interactions between neighboring conjugated moieties that result in intermolecular aggregation and the formation of close packed crystalline domains.<sup>[25]</sup> Even when successful in inducing phase-separation, these approaches typically introduce no cohesive forces capable of stabilizing the processed blend in a desired optimized morphology. The resulting phase separation is therefore inherently unstable and subject to changes due to temperature or to the exposure to environmental agents, such as moisture or solvents. To date, fine control of phase separation represents the most critical challenge for boosting the efficiency of SM-BHJ solar cells. Specifically, in contrast to polymer BHJs where the film morphology and segregation can be finely controlled through simple annealing procedures owing to the low molecular mobility of long polymeric chains, thermal annealing of small-molecule BHJs leads to rapid and therefore less controllable segregation that may result in suppression of exciton splitting and consequent reduction of photovoltaic activity<sup>[26]</sup> (see Supporting Information).

Here we demonstrate a new paradigm for external fine control of phase segregation in SM-BHJs that raises the device efficiency of over twenty times with respect to unprocessed devices. Our strategy consists in the post-deposition activation of a network of latent hydrogen-bonds (H-bonds) between

functionalized donor molecules blended with PCBM through thermally induced decomposition of labile protecting groups that prevent the H-bonding from occurring in the as-deposited films.

This concept was initially introduced for increasing the solution processability of molecular pigments<sup>[27,28]</sup> and, more recently, it has been applied to increase the charge mobility in ambipolar organic transistors through the formation of highly ordered molecular arrangements.<sup>[29]</sup> The key aspect of the approach, schematically depicted in **Figure 1a**, is the temporary ‘deactivation’ of the H-bond-forming sites of the donor molecule by its protection with a thermally labile functionality. This makes the donor miscible with PCBM in common solvents, allowing for the use of conventional solution-based deposition methods on transparent conductive substrates. The formation of phase segregated domains is successively finely tuned by thermal cleavage of the protective group and consequent activation of the H-bonding sites. Through this approach, we can control the blend morphology from the initial kinetic structures formed during film deposition (i.e., evaporation of the solvent during spin-coating) all the way to thermodynamic macrophase-separated materials and thereby access intermediate morphologies that simultaneously optimize the charge separation efficiency at the donor/acceptor interfaces and charge mobility through the formation of interpenetrated phase separated percolation pathways.

## 2. Results and Discussion

In our work we used a functionalized diketopyrrolopyrrole (DPP) derivative as electron donor blended with a conventional PCBM acceptor. DPP derivatives have recently received considerable attention as efficient donor materials thanks to their high polarizability and good self-assembly properties arising from their planar conjugated bi-cyclic structure that promotes  $\pi$ - $\pi$  interaction in the solid state.<sup>[30]</sup> Furthermore, the electron withdrawing DPP core can be functionalized with electron rich substituents, which confer to the molecule a donor–acceptor–donor (D-A-D) character. The resulting intramolecular charge transfer process provides an additional mean to tune the absorption spectrum so as to cover the whole visible spectral region.<sup>[31]</sup>

Our molecule of choice is di-*tert*-butyl-3,6-di(biphenyl-4-yl)-1,4-dioxopyrrolo[3,4-c]pyrrole-2,5(1*H*,4*H*)-dicarboxylate (hereafter referred to as DPP<sub>H</sub>), a D-A-D functionalized DPP whose lactamic nitrogens are protected by *tert*-butoxycarbonyl (t-BOC) groups (highlighted in red in **Figure 1b**). The decomposition of the t-BOC functionalities into gaseous species (CO<sub>2</sub> and isobutene) triggers the formation of H-bonds between neighboring DPP<sub>H</sub> molecules leading to the desired phase segregation. Morphological and structural analyses reveal the gradual evolution of the amorphous and uniform pristine film into a mosaic of segregated crystalline domains. The separation of donor and acceptor species is confirmed by spectroscopic measurements that show the progressive increase of the DPP<sub>H</sub> luminescence in thermally treated (“deprotected”) films, index of slightly reduced ultrafast exciton splitting that instead completely quenches the emission of the pristine ‘protected’ blend. Despite the partially suppressed exciton splitting

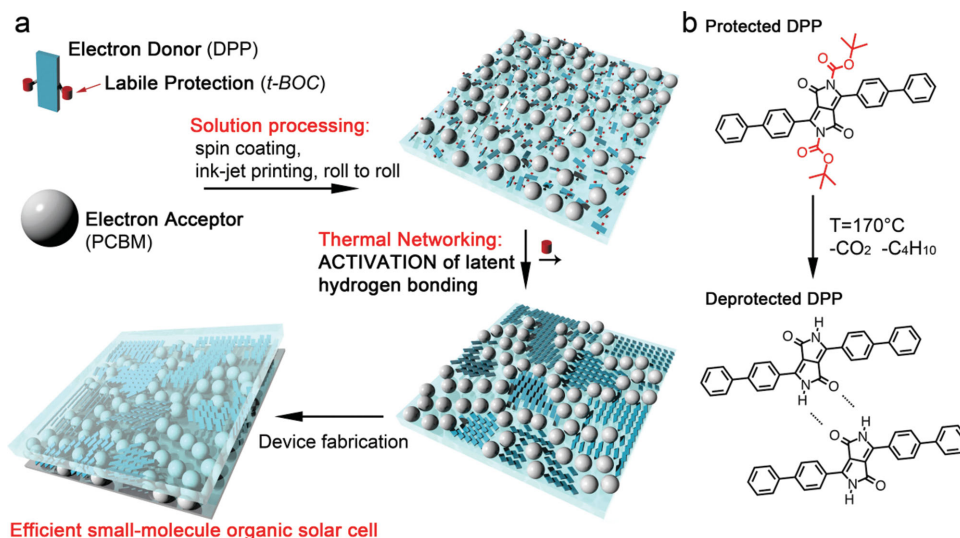


**Figure 1.** Concept of latent H-bonding activated phase segregation in SM-BHJs. a) Schematic representation of the latent H-bonding strategy in the fabrication of SM-BHJ solar cells. A solution of protected donor and acceptor molecules is deposited on transparent conductive substrates via a simple solution process (i.e., spin coating, roll-to-roll/ink-jet printing). The post-deposition thermal treatment removes the thermolabile protective functionalities thereby activating the latent H-bonding sites. As a result, the donor moieties network, leading to a fine controlled phase segregated polycrystalline film. Deposition of the extraction electrodes is carried out by standard procedures. b) Activation of latent H-bonding in di-*tert*-butyl 3,6-di(1,1'-biphenyl-4-yl)-1,4-dioxopyrrolo[3,4-c]pyrrole-2,5(1*H*,4*H*)-dicarboxylate. At 170 °C the *ter*-butoxycarbonyl (*t*-BOC) protection group (highlighted in red) is converted in carbon dioxide (CO<sub>2</sub>) and isobutene (C<sub>4</sub>H<sub>10</sub>).

in phase segregated films, the improved charge mobility leads to a dramatic increase of the short circuit current, and thereby boosts the power conversion efficiency up to twenty times that of pristine devices. In order to unambiguously ascribe the observed improvement of the PV performances to the activation of latent H-bonding network, we synthesized a control molecule, 3,6-di(biphenyl-4-yl)-2,5-bis(2-ethylhexyl)-2,5-dihydropyrrolo[3,4-c]pyrrole-1,4-dione (referred to as DPP<sub>C</sub>, see Supporting Figure S1) with similar structure to DPP<sub>H</sub> except for the protection of the lactamic nitrogens which, in this case, is provided by 2-ethylhexyl alkyl chains that are stable at the processing temperature and thus unaffected by the thermal treatment. Thermal annealing of the control blends leads to minor changes in the film structure that remains amorphous and to the disruption of the photovoltaic activity, most likely due to uncontrollable complete segregation of DPP<sub>C</sub> molecules in nearly pure amorphous domains.

### 2.1. Thermal Activation of Intermolecular Aggregation

We start our study by providing evidence of controlled thermal decomposition of the *t*-BOC protective functionality and consequent formation of intermolecular DPP<sub>H</sub> aggregates. In **Figure 2a** we report the thermogravimetric analysis (TGA) of DPP<sub>H</sub> powder and the respective mass release curves as obtained through coupled mass spectroscopy measurements on the exhaust gases. At 200 °C, a first 29% weight loss is observed with concomitant emission of CO<sub>2</sub> and C<sub>4</sub>H<sub>10</sub>, as expected for the thermal cleavage of the protective *t*-BOC group. DPP<sub>H</sub> is otherwise stable up to 500 °C where a further 40% mass loss and corresponding CO<sub>2</sub> emission indicates the degradation of the DPP core.

The thermogram provides an indication of the thermal budget necessary to convert DPP<sub>H</sub> into its deprotected form. In order to fine tune the thermal activation of hydrogen networking, we chose to provide the required thermal budget by heating the samples at 170 °C, which is slightly below the peak deprotection temperature of ≈200 °C. This allows us to slow down the hydrogen networking process and thereby to control its extent through the duration of the thermal treatment, hereafter expressed in terms of thermal treatment time (*t*<sub>TT</sub>).

Thermal deprotection and consequent activation of H-bonding sites is confirmed by Fourier transform infrared (FT-IR) transmission measurements that allow us to monitor the evolution of the functional groups in the film at different stages of the thermal treatment (**Figure 2b**) through the intensity of their characteristic vibrational modes. Upon annealing, the characteristic signal of the C = O stretching mode at 1740 cm<sup>-1</sup> is reduced to below 50% of its initial intensity, indicating the successful removal of the *t*-BOC protective groups (the residual signal is due to the C = O bond of PCBM). Most importantly, the characteristic signal of the N-H stretching mode between 3000 cm<sup>-1</sup> and 3200 cm<sup>-1</sup> concomitantly grows, confirming the activation of H-bonding sites.

As a result of thermal deprotection, DPP<sub>H</sub> moieties progressively aggregate both in pure and blended films. **Figures 2c** and **2d** show the absorption spectra of a pure DPP<sub>H</sub> film and of a 1:1 DPP<sub>H</sub>:PCBM blend as a function of the thermal treatment time, *t*<sub>TT</sub> = 0–1000 s. The pristine DPP<sub>H</sub> film (**Figure 2c**) shows a first absorption band at about 2.7 eV that well resembles the absorption profile of the diluted solution (Supporting Information **Figure S2**) and is therefore ascribed to non-interacting DPP<sub>H</sub> molecules.<sup>[26]</sup> The thermal deprotection induces a progressive drop of the 2.7 eV absorption feature with increasing *t*<sub>TT</sub>, accompanied by the growth of a lower energy

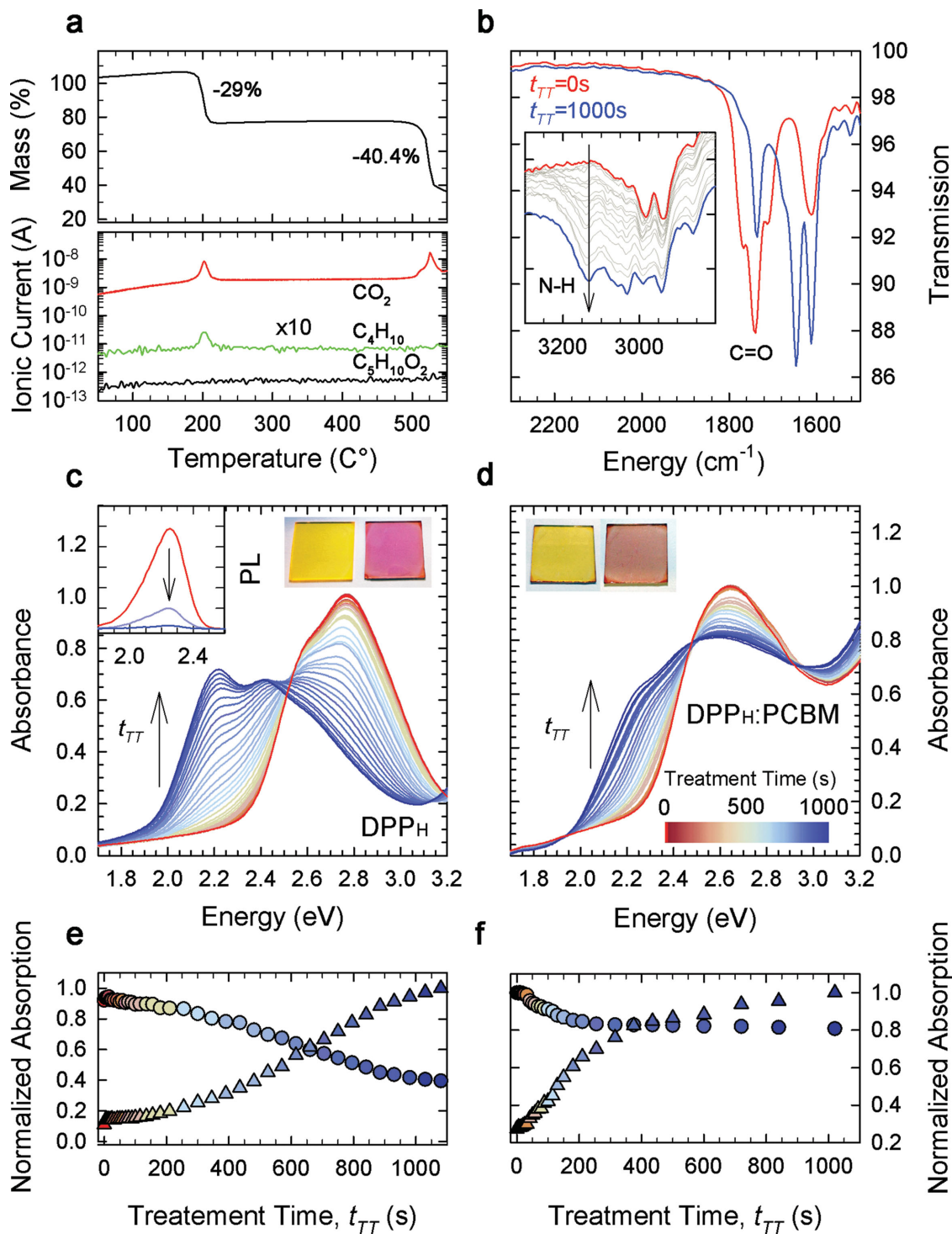


**Figure 2.** Thermogravimetric, UV-Vis absorption and FT-IR analyses. a) Thermogravimetric analysis (TGA) of DPP<sub>H</sub> powder performed under nitrogen atmosphere (upper panel) and related mass release curves (lower panel) identifying the emission of CO<sub>2</sub> (red line), C<sub>4</sub>H<sub>10</sub> (green line) and C<sub>5</sub>H<sub>10</sub>O<sub>2</sub> (black line). The green curve has been shifted upwards by 10 times for clarity. b) IR transmission spectra of pristine (red line) and fully converted ( $t_{TT} = 1000$  s, blue line) DPP<sub>H</sub>:PCBM films (1:1 wt%) showing the drop of the C=O stretching mode upon thermal deprotection. Inset: IR transmission spectra in the 2800–3300 cm<sup>-1</sup> region characteristic of N-H stretching mode. Absorption spectra of c) a pure DPP<sub>H</sub> film and of d) a DPP<sub>H</sub>:PCBM (1:1 wt%) blend for increasing treatment time,  $t_{TT}$  (indicated by the arrow). The photoluminescence spectra of the pure DPP<sub>H</sub> film excited at 400 nm are shown in the inset ( $t_{TT} = 0$  s, red line;  $t_{TT} = 30$  s, purple line;  $t_{TT} = 480$  s, blue line;) together with the photographs of the samples before (yellow films) and after 1000 s thermal treatment at 170 °C (brown films). e) Normalized absorption at 2.2 eV (circles) and at 2.7 eV (triangles) as a function of  $t_{TT}$  extracted from (c, d) for e) the pure DPP<sub>H</sub> film and f) the DPP<sub>H</sub>:PCBM blend. The same color code applies throughout panels (b–f).

band at 2.2 eV ascribed to molecular aggregates, with a clear isosbestic point at 2.5 eV. Accordingly, the DPP<sub>H</sub> photoluminescence (PL) is progressively quenched (inset of Figure 2c), possibly due to increased exciton mobility in the aggregated film that allows excitons to rapidly reach non-radiative quenching sites. Similar evolution of the absorption spectrum is observed for the blended film where the absorption profile of DPP<sub>H</sub> is overlapped to the absorption spectrum of PCBM. Also in this case, the thermal treatment leads to progressive growth of the absorption band at 2.2 eV, thus confirming that DPP<sub>H</sub> moieties aggregate following deprotection also in the blended film. To semi-quantitatively monitor the combined deprotection/aggregation process, in Figure 2e,f we report the intensity of the characteristic absorption bands as a function of  $t_{TT}$  for both films. In both cases, the evolution of the absorption features at 2.2 eV and 2.7 eV is anti-correlated, indicating a progressive conversion of isolated DPP<sub>H</sub> moieties into intermolecular aggregates of deprotected species. We note that the growth of the aggregate band is faster in the blend than in the pure DPP<sub>H</sub> film, which suggests a role of PCBM in promoting the formation of DPP aggregates and/or the cleavage of the protecting group. In contrast, UV-Vis absorption measurements on control films of pure DPP<sub>C</sub> and DPP<sub>C</sub>:PCBM 1:1 blend show no aggregate band at any  $t_{TT}$  (Supporting Information Figure S3), thus confirming the key role of H-networking activated by thermal removal of the t-BOC protection as a driving force for intermolecular aggregation in the solid state.

## 2.2. Morphological and Structural Analyses

As mentioned above, the key advantage of the proposed strategy is the ability to externally tune the film morphology and phase segregation through the thermal activation of latent H-bonds. To demonstrate the control over film morphology and crystal structure we performed atomic force microscopy (AFM) and X-ray diffraction (XRD) measurements on pure DPP<sub>H</sub> and blended films at different stages of thermal treatment. Figure 3a,b report the AFM images and XRD patterns of a 100 nm DPP<sub>H</sub>:PCBM (1:1) film on a Si(100) substrate both as-spun and for  $t_{TT}$  up to 510 s (the same analysis for a pure DPP<sub>H</sub> film is reported in Supporting Figure S4). The pristine film shows uniform morphology with roughness (rms) below 1 nm and no evident diffraction signal, indicating a substantially amorphous state. After a 30 s thermal treatment, the film surface becomes structured with the formation of elongated lamellar domains with thickness of about 1 nm. The surface roughness undergoes a three-fold increase with respect to its initial value (see Supporting Information Table S1). The XRD pattern shows a sharp diffraction peak at  $2\theta = 7.6^\circ$  (with replicas up to the fifth order) which are indicative of the development of a crystalline phase with the highest out-of-plane periodicity with spacing of 1.12 nm, consistent with the morphological features observed in the respective AFM image. Extended treatments up to  $t_{TT} = 270$  s induce a further increase in crystallinity and the formation of 10–20 nm three-dimensional crystalline domains. We note that, while the volume fraction of the crystalline phase grows, resulting in more intense XRD signal, the diffraction peak is substantially

broader with respect to shorter treatments, which indicates the polycrystalline nature of the film. Further annealing has a detrimental effect on the surface morphology as the XRD signal broadens and drops in intensity accompanied by a substantial blurring of the morphologic features. Literature reports cases of surface induced polymorphism in DPP films, which might play a role in the further evolution of the annealed crystalline domains.<sup>[32]</sup> The whole process is in any case fully reproducible and thus controllable at any required treatment timescale. Interestingly, the maximum crystallinity is observed for  $t_{TT} = 270$  s (Figure 3c), corresponding to the most interpenetrated morphology evidenced by the AFM images. The same evolution of the film structure is observed for pure DPP<sub>H</sub> films while pure PCBM films are unaffected by the thermal treatment (Supporting Information Figure S4,S5). This suggests that the presence of PCBM does not sensibly interfere with the thermal activation of the H-network, in agreement with the optical absorption measurements reported in Figure 2.

Importantly the film morphology and crystallinity are preserved for shelf times up to 6 months. As shown in Figure 4a, the XRD pattern of a representative DPP<sub>H</sub>:PCBM film stored in air under ambient illumination for over 6 months shows an intense diffraction peak at  $2\theta = 7.6^\circ$  and surface morphology as a blend measured immediately after the thermal deprotection (Figure 3). This further emphasises the ability of the thermally activated H-network to stabilize the blend nanoarchitecture for extended periods of time in lighting conditions at room temperature. Furthermore, as a result of the strong cohesive forces introduced by the H-bonds, the processed blend becomes essentially insoluble in common solvents (Figure 4b), similarly to what observed with latent pigments used in inks and varnishes.<sup>[27]</sup> Specifically, in Figure 4b, we report the optical absorption spectra of pristine and deprotected blends before and after washing in water, ethanol and acetone. Remarkably, while the pristine films are dissolved by ethanol and acetone, their deprotected analogues are unaffected by the washing procedure.

Finally, we performed AFM and XRD analyses on 1:1 DPP<sub>C</sub>:PCBM control blends (Supporting Information Figure S6,S7). The morphology of the pristine control film is smooth and shows no mesoscopic phase segregation. In strong contrast with the DPP<sub>H</sub>-based films, the surface smoothness is preserved up to  $t_{TT} = 270$  s, when isolated cap-shaped aggregates emerge. XRD measurements show that the film remains completely amorphous throughout the whole range of  $t_{TT}$  investigated ( $t_{TT} = 0$  s to  $t_{TT} = 510$  s), thus indicating that eventual phase-separation in the absence of H-network is not accompanied by preferential structural ordering.

## 2.3. Hydrogen-networked SM-BHJ Solar Cells

To experimentally validate the concept of post deposition activation of latent H-bonding for improving the performances of SM-BHJ solar cells, we fabricated and tested simple proof-of-principle devices consisting of a 100 nm DPP<sub>H</sub>:PCBM (70:30 wt%) film at different stages of thermal treatment sandwiched between an ITO/PEDOT:PSS anode and a LiF/Al cathode (1.5 nm LiF, 90 nm Al). The electrical response of the

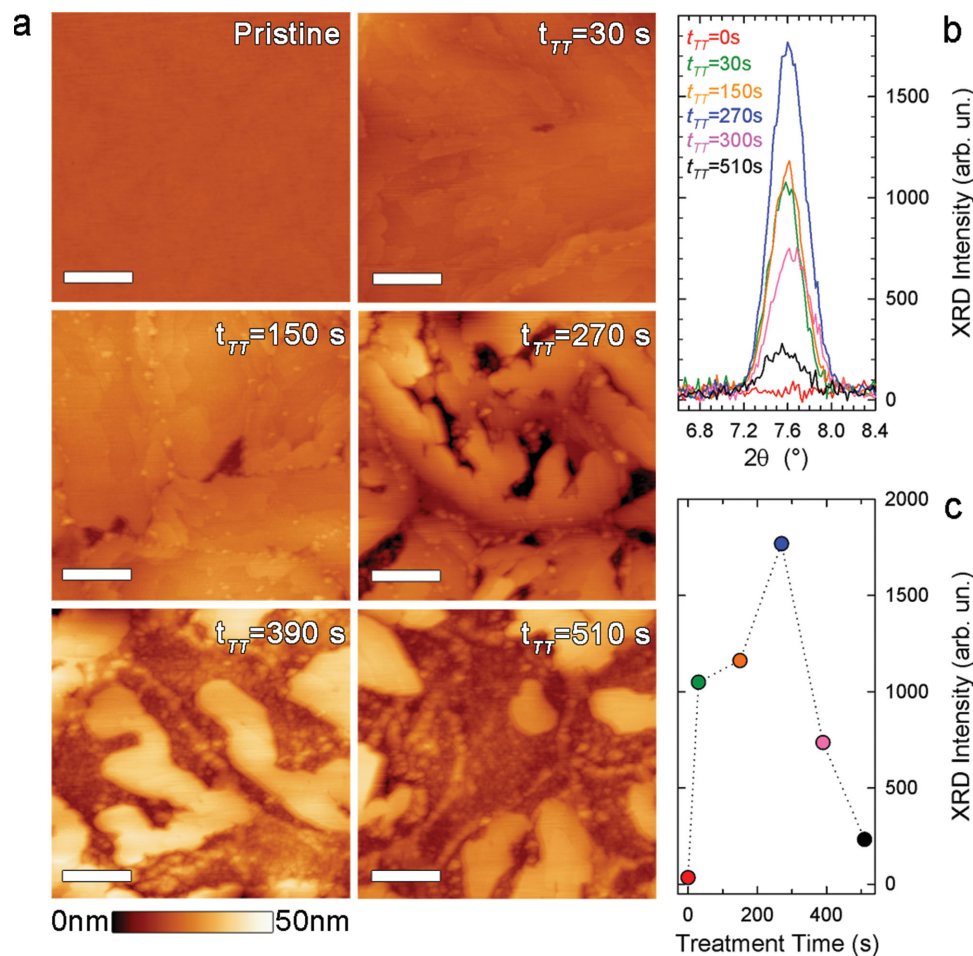


**Figure 3.** H-networked SM-BHJ morphology and structure. Development of crystalline phase segregated domains through activation of latent H-bonds in DPP<sub>H</sub>:PCBM blends. a) AFM surface topography of DPP:PCBM (1:1 wt%) films on Si(100) substrates as measured at room temperature after thermal treatments performed for the time reported on the top-right of each panel. The white scale bar corresponds to 400 nm. The corresponding surface roughness is reported in Supporting Information Table S1. b) X-ray diffraction patterns for the same films as in 'a' showing the XRD peak corresponding to the out-of-plane spacing  $d = 1.12$  nm of the crystal phase of unprotected DPP<sub>H</sub>. c) Evolution of the integrated intensity of the peak with thermal treatment time. The same color code applies throughout the figure.

devices under AM 1.5G illumination is reported in **Figure 5a**, showing negligible dependence of the open circuit voltage ( $V_{OC}$ ) on  $t_{TT}$ , a further evidence that the conjugated structure of the DPP<sub>H</sub> core is preserved upon thermal deprotection. Remarkably, the short circuit current density ( $J_{SC}$ ) shows a 30-fold increase upon annealing for  $t_{TT} = 270$  s, resulting in the concomitant growth of the power conversion efficiency (PCE) to  $\approx 0.15\%$ , which is over 20 times larger than the efficiency of the pristine device (Figure 5b). The electrical characteristics of the best performing device of each set are reported in Supporting Information Table S2.

The same study performed on control solar cells based on a DPP<sub>C</sub>:PCBM (70:30 wt) blend shows that, while the pristine device has similar PCE to its DPP<sub>H</sub>:PCBM counterpart, the device treated for  $t_{TT} = 270$  s exhibits no PV activity (Supporting Information Figure S8 and Table S3). This unambiguously demonstrates that the deprotection of the DPP<sub>H</sub> molecules and the consequent H-networking play a key role in improving the PV performances of our solar cells. We note

that these proof-of-principle devices have not been optimized for high absolute efficiency in terms of the active layer thickness, electrodes work functions and donor/acceptor ratio. Improved performances can potentially be achieved by tuning the DPP energy levels and optical gap, so as to better cover the solar spectrum and improve charge separation. In fact, as shown by the energy levels diagram in Figure 5b, the highest occupied molecular orbital (HOMO) level of DPP<sub>H</sub> is slightly lower than the HOMO of PCBM ( $-6.22$  eV vs  $-6.1$  eV) which results in poor charge separation at the hetero interface. Several examples of BHJ solar cells based on DPP derivatives have been reported achieving conversion efficiencies up to 4%.<sup>[30,33]</sup> We therefore expect significant improvements by applying the proposed strategy to optimized molecular systems. The latent pigment strategy can also be extended to other classes of high performance pigments such as quinaclidone and isoindigo.<sup>[34]</sup> Further optimization can also be achieved through the implementation of more complex device architectures.<sup>[6,8]</sup>

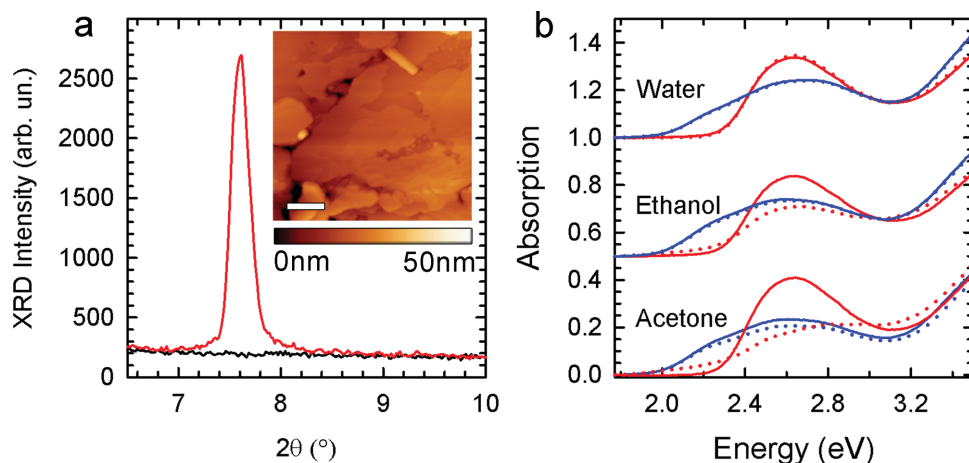


**Figure 4.** Stability. a) Diffraction patterns of DPP<sub>H</sub>:PCBM (1:1 wt%) films on silica substrates at  $t_{TT} = 270$  s after a shelf time of 6 months (pristine – black line, treated for  $t_{TT} = 270$  s – red line). The inset shows the AFM surface topography of the same sample. The scale bar corresponds to 400 nm. b) UV–Vis absorption spectra of pristine (red) and treated ( $t_{TT} = 270$  s, blue) DPP<sub>H</sub>:PCBM films before (continuous line) and after (dotted line) washing in various solvents. The spectra of the films washed in water and ethanol have been shifted up for clarity. ‘Deprotected’ blends are essentially insoluble in any of the solvents tested due to H-networking that introduces strong cohesive forces which dramatically improve the stability of the film with respect to common untreated films.

To gather a deeper insight into the role of the molecular aggregates in deprotected crystalline films on the production of photocurrent, we measured the spectrally resolved incident

photon-to-current efficiency (IPCE) of the same solar cells as in Figure 5a,b. In Figure 5c,d we report the optical absorption and the IPCE spectrum of a pristine device and of a cell treated for

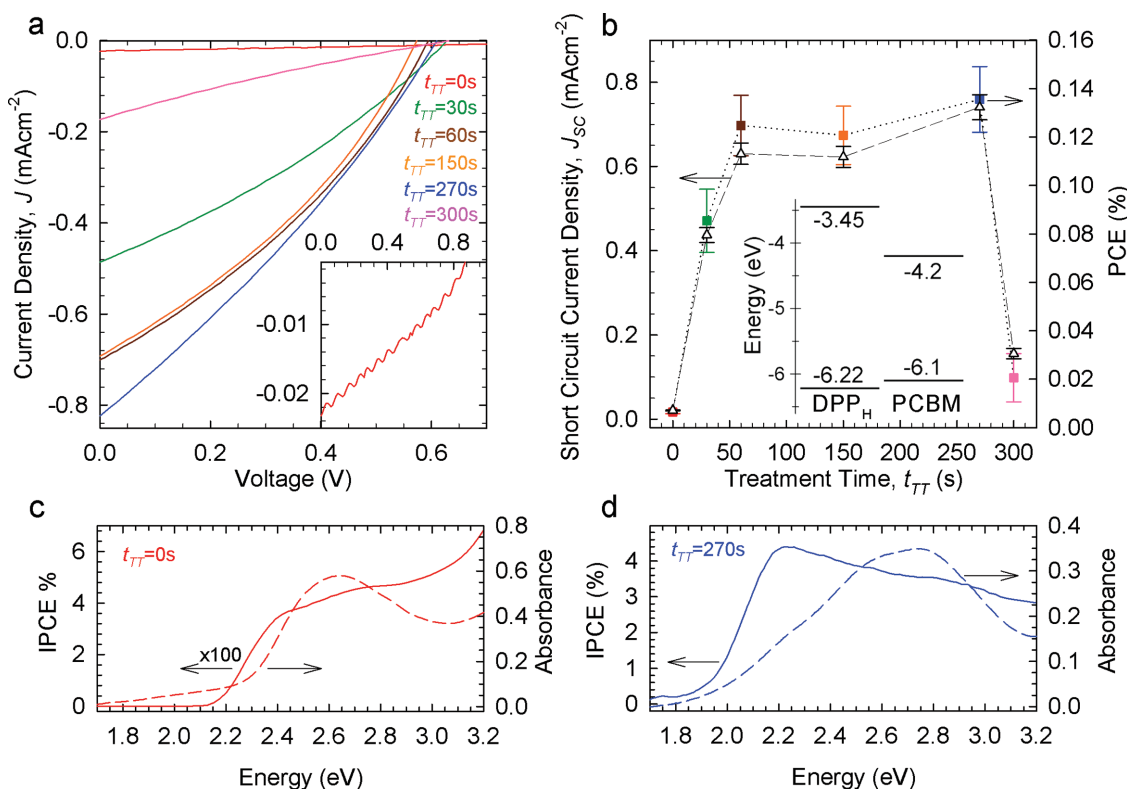


**Figure 5.** H-networked SM-BHJ solar cells a) Current density–voltage (JV) responses of SM-BHJ solar cells incorporating a 100 nm thick DPP<sub>H</sub>:PCBM (70:30 wt%) film treated for  $t_{TT} = 0, 30, 60, 150, 270, 300$  s under AM 1.5G illumination ( $100 \text{ mW/cm}^2$ ). Inset, zoomed-in JV response of unprocessed device. b) evolution of the short circuit current density (triangles) and power conversion efficiency (PCE, squares) with  $t_{TT}$ . Symbols are the mean values averaged over 10 devices and error bars represent the respective standard deviation. Schematic diagram of the energy levels of DPPH and PCBM are reported in the inset. Absorption spectrum (continuous line) and IPCE (dashed line) spectra for c) a SM-BHJ solar cell incorporating a pristine DPP<sub>H</sub>:PCBM (70:30 wt%) film (red lines) and d) the same blend treated for 270 s (blue lines). The same color code applies throughout the figure.

$t_{TT} = 270$  s. As expected, the IPCE spectrum of the “protected” device resembles well its absorption spectrum with no evident contribution of intramolecular aggregates at 2.2 eV. On the other hand, the IPCE spectrum of the ‘deprotected’ cell shows a marked band at 2.2 eV that is significantly more intense than the corresponding optical absorbance, indicating that intermolecular aggregates more efficiently convert absorbed light into photocurrent with respect to isolated molecules.

## 2.4. Photophysical Investigation of Thermally Induced H-Networking

Finally, we use time-resolved photoluminescence experiments to probe the phase separation on a molecular scale and thereby to unravel the photophysical processes underpinning the improved efficiency in H-networked SM-BHJ solar cells. Figure 6a–c shows the time-integrated PL spectra and the PL decay curves of a DPP<sub>H</sub>:PCBM blend at increasing  $t_{TT}$ . The corresponding contour plot of PL decay traces versus  $t_{TT}$  is reported in Figure 6d. A schematic representation of the photophysical processes occurring in the film at different stages of thermal treatment is depicted in Figure 6e. In the as-spun DPP<sub>H</sub>:PCBM blend, donor and acceptor molecules are finely mixed and the recombination of DPP<sub>H</sub> excitons is dominated by ultrafast electron transfer to PCBM (Figure 6e<sup>I</sup>). Accordingly, the film is completely non emitting. Brief thermal treatments

lead to the formation of amorphous phase-segregated domains rich in DPP<sub>H</sub> and PCBM (see Figure 3). In this film morphology, DPP<sub>H</sub> excitons are photogenerated sufficiently far from PCBM to be able to recombine radiatively before reaching the domain interfaces where they are split by ultrafast electron transfer. As a result, the film becomes progressively more emissive (zone “1” in Figure 6b) and the PL decay curve shows the typical stretched exponential behavior that reflects the distribution of distances between the photoexcitation spot and the quenching site (i.e., the DPPH/PCBM interface) characteristic of the diffusion limited recombination regime (Figure 6c).<sup>[17,35]</sup> The increase of crystallinity observed in XRD analyses for extended treatments enhances the exciton mobility in the DPP<sub>H</sub>-rich domains leading to faster exciton diffusion and consequent quenching of the PL by electron transfer to PCBM or by nonradiative decay in defect sites (zone “2” in Figure 6b, e<sup>II</sup>). Fast migration to the donor–acceptor interfaces and consequent shorter PL lifetime in films subject to treatments between 200 s and 300 s is confirmed by both the more pronounced fast PL decay component in Figure 6c and by the accumulation of isolines in the contour plot in Figure 6d. Finally, longer thermal treatments induce the progressive amorphization of the film which suppresses exciton mobility (Figure 6e<sup>IV</sup>) and leads to the slow recover of the emission yield (zone “3” in Figure 6b). As a result of hindered exciton diffusion, the decay kinetics becomes single exponential with lifetime  $\approx 800$  ps comparable to that of pure DPP<sub>H</sub> film (Supporting Information Figure S9),

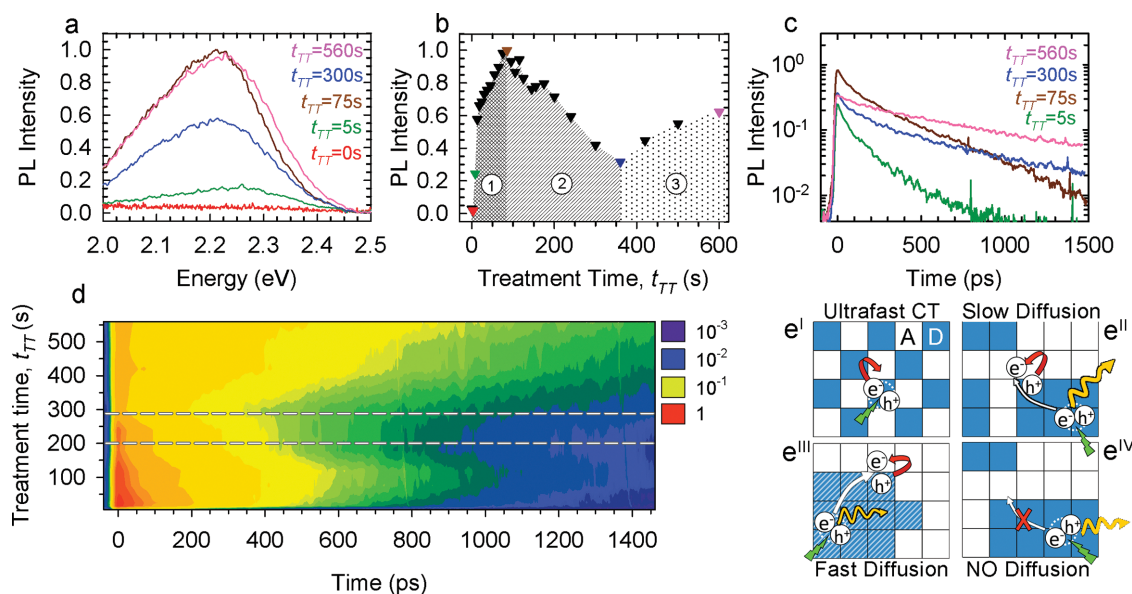


**Figure 6.** Photophysical study of H-networked SM-BHJs a) PL spectra, b) integrated PL intensity and c) PL decays of a DPP<sub>H</sub>:PCBM (1:1 wt%) film for different treatment time. The same color code applies throughout panels (a–c). d) Contour plot of the PL decays as a function of  $t_{TT}$  (logarithmic scale). The dashed lines highlight the region corresponding to the highest exciton mobility. e) Schematic representation of the photophysical processes occurring in the film at the different stages of the thermal deprotection: e<sup>I</sup>) In the as-spun film, DPP<sub>H</sub> donors (D, blue squares) and PCBM acceptors (A, white squares) are finely mixed. Photogenerated excitons are rapidly split by ultrafast charge transfer (red arrow) and no PL is observed; e<sup>II</sup>) The progressive growth of DPP<sub>H</sub>-rich domains due to the ongoing phase segregation process makes radiative exciton relaxation the dominant recombination process, leading to progressively more intense PL (yellow arrow, corresponding to zone “1” in panel (b)); e<sup>III</sup>) Crystallization of the phase-separated domains (highlighted in striped blue/green) favors the mobility of excitons in the film and, consequently, their diffusion (white arrows) to the donor–acceptor interfaces. As a result, rapid electron transfer competes with radiative exciton recombination leading to the gradual drop of the PL intensity observed in zone “2” of panel (b); e<sup>IV</sup>) Amorphization of the film for prolonged thermal annealing suppresses exciton diffusion leading to the progressive recover of the PL (corresponding to zone “3” in panel “b”).

indicating that the dominant decay process is now the radiative recombination of excitons in the large DPP<sub>H</sub>-rich domains.

Importantly, the PL drop due to increased exciton mobility observed for  $t_{\text{TT}} \approx 270$  s correlates remarkably well with the maximum crystallinity and the higher power conversion efficiency shown in Figure 3, 5. It is also worth noting that higher PCE are obtained despite the fact that the phase segregation process induced by thermal activated H-networking reduces the exciton splitting efficiency by increasing the size of the DPP<sub>H</sub>- and PCBM-rich domains, as shown by the higher zero delay PL intensity in deprotected films for  $t_{\text{TT}}$  up to 75 s, with respect to their pristine form. This, together with the higher current density flowing through the device, further demonstrates that the improvement of PV performances is mainly due to the larger charge mobility in the H-networked blends, which overcompensates the slightly lower number of free carrier generated in the phase-separated film.

### 3. Conclusions

In conclusion we demonstrated a novel approach to fine control the phase segregation of solution processed SM-BHJ solar cells based on the exploitation of latent H-bonding via thermal deprotection of electron donor DPP derivatives blended with PCBM. As shown by AFM and XRD analyses, the thermally induced H-networking of the DPP molecules provides the necessary driving force for the formation of interpenetrated crystalline domains rich in donor and acceptor moieties, resulting in over 20-fold increase of the PV efficiency. The improvement of the PV performances in the SM-BHJ solar cells is due to a larger short-circuit current resulting from the higher carrier mobility in the crystalline aggregates of deprotected DPP molecules, in agreement with the higher exciton mobility highlighted by time-resolved photoluminescence experiments. The demonstrated approach to controlled post-deposition phase segregation in SM-BHJ solar cells, demonstrated here for DPP derivatives blended with PCBM, could be extended to smaller band gap molecular semiconductors for achieving a better match with the spectrum of solar radiation and thereby strongly boost the PV efficiency of small-molecule solar cells.

### 4. Experimental Section

**Materials:** Both DPP<sub>H</sub> and DPP<sub>C</sub> were prepared starting from the corresponding pigment 3,6-di(biphenyl-4-yl)pyrrolo[3,4-c]pyrrole-1,4(2H,5H)-dione (**1**). Derivative DPP<sub>C</sub> was obtained according to the common procedure of alkylation of DPP derivatives by reacting **1** with 2-ethylhexyl iodide.<sup>[66]</sup> DPP<sub>H</sub> was prepared by a modification of the literature procedure.

**Synthesis of di-tert-butyl 3,6-di(biphenyl-4-yl)-1,4-dioxopyrrolo[3,4-c]pyrrole-2,5(1H,4H)-dicarboxylate (DPP<sub>H</sub>):** In an Ar filled glove box, a suspension of **1** (1.000 g, 2.270 mmol) and DMAP (693 mg, 5.672 mmol) in anhydrous THF (20 mL) is prepared and stirred at room temperature for 15 min. A solution of di-tert-butyl dicarbonate (2.480 g, 11.36 mmol) in THF (8 mL) is added and the mixture is stirred at room temperature for 46 h. A yellow suspension is obtained. Light petroleum ether (30 mL) is added and the mixture is stirred for 30 min and filtered obtaining a yellow solid. Product is dissolved in CH<sub>2</sub>Cl<sub>2</sub> and filtered through a short silica plug. Solvent is evaporated under reduced pressure obtaining

pure product as a yellow solid (1.186 g, 1.948 mmol, yield 85.8%). Characterizations are in agreement with those previously reported.<sup>[37]</sup>

**Electrochemical Analysis:** 20 mg of t-BOC protected DPP<sub>H</sub> were dispersed in 1 mL of CH<sub>2</sub>Cl<sub>2</sub>. The suspension was filtered to obtain a saturated solution and casted on the top of a well polished glassy carbon tip working electrode (surface area 0.071 cm<sup>2</sup>). A thin molecular film of DPP<sub>H</sub> was then obtained by solvent evaporation at room temperature and thermal treatment (20 min at 170 °C). The glassy carbon supported film was characterized by Differential Pulsed Voltammetry in tetrabutylammonium perchlorate 10<sup>-1</sup> M in anhydrous acetonitrile at 20 mV/s. The counter, and pseudoreference electrodes were a Pt flag and a Ag/AgCl wire, respectively. The Ag/AgCl pseudoreference electrode was externally calibrated by adding ferrocene (10<sup>-3</sup> M) to the electrolyte ( $E_{1/2} = 0.39$  V,  $\Delta E = 62$  mV). Measurements were carried out in a glove box filled with argon ([O<sub>2</sub>] < 1 ppm). LUMO energies was calculated by the DPV peak potential value considering the Fc vacuum level at -5.23 eV.

**Structural and Morphological Analyses:** X-ray diffraction specular scans on single crystals and films were performed with a PANalytical X'Pert Pro powder diffractometer with Cu K $\alpha$  radiation. AFM images were obtained with a Nanoscope V MultiMode atomic force microscope (Veeco) using single-beam silicon cantilevers (force constant of 40 N/m) operating in intermittent contact (tapping) mode. Image analysis was performed with the program WSXM.

**Solar Cells Fabrication and Characterization:** For the preparation of solar cells, indium tin oxide (ITO)-coated glass substrates were sonicated for 10 min in isopropanol and treated in a nitrogen plasma chamber for 10 min. A layer of poly(3,4-ethylene dioxythiophene)/poly(styrene - sulfonate) (PEDOT:PSS, ClevisP VP.AI 4083) was spin coated from aqueous solution. The film was annealed under nitrogen atmosphere at 150 °C for 15 min. Profilometric measurements of the PEDOT:PSS layer reported a thickness of 40 nm. A 20 mg/mL chloroform solution of DPP and [60]PCBM (Solenne B.V., The Netherlands) 70:30 wt. was stirred overnight and then filtered through a 0.22  $\mu$ m poly(tetrafluoroethylene) PTFE filters. The solution was spin coated on the ITO PEDOT:PSS substrates at 1500 rpm for 60 s which yielded a film  $\approx$ 100 nm thick. A lithium fluoride layer (1.5 nm) coated with aluminium (100 nm) was thermally evaporated using a shadow mask. Current versus voltage curves (*I*-*V*) characteristics were measured with a Keithley 2602 Digital Source Meter. The cells were illuminated from the glass side with a 100 mW/cm<sup>2</sup> ABET Technologies Sun 2000 Solar Simulator. No mask was used in the *I*-*V* measurements. An average of ten devices per treatment time were characterized. Spectrally resolved incident photon-to-current efficiency (IPCE) was recorded by illuminating the solar cells with calibrated monochromatic light from a Xe lamp coupled to a monochromator. All fabrications and characterizations were performed under nitrogen.

**Spectroscopic Studies:** Spectroscopic measurements were performed on diluted chloroform solution and spin coated films on silica substrates. IR spectroscopy was performed with a  $\mu$ -FTIR Nicolet iN 10. Absorption spectra were collected with a Varian Cary 50 spectrophotometer. Time-resolved PL measurements were carried out using 410 nm (3.02 eV) excitation from a doubled Ti:Sapphire laser (Coherent Mira 900), and detecting the emitted light with an Hamamatsu C4742-95 streak camera.

### Acknowledgements

S.B., F.M., and U.G. acknowledge support from Cariplo Foundation (2012-0844). L.B. and M.S. acknowledge support from Cariplo Foundation (2010-1832). S.B. wishes to thank the European Community's Seventh Framework Programme (FP7/2007-2013) under grant agreement N. 324603 for financial support (EDONHIST). The authors thank Dr. A. Colombo for technical assistance in TGA and mass spectrometry experiments.

Received: March 19, 2014

Revised: June 13, 2014

Published online:

- [1] a) C. J. Brabec, S. Gowrisanker, J. J. M. Halls, D. Laird, S. J. Jia, S. P. Williams, *Adv. Mater.* **2010**, *22*, 3839; b) A. J. Heeger, *Adv. Mater.* **2014**, *26*, 10; c) S. Gunes, H. Neugebauer, N. S. Sariciftci, *Chem. Rev.* **2007**, *107*, 1324; d) A. M. Ballantyne, L. Chen, J. Dane, T. Hammant, F. M. Braun, M. Heeney, W. Duffy, I. McCulloch, D. D. C. Bradley, J. Nelson, *Adv. Funct. Mater.* **2008**, *18*, 2373; e) B. C. Thompson, J. M. J. Fréchet, *Angew. Chem. Int. Ed.* **2008**, *47*, 58.
- [2] a) M. Kaltenbrunner, M. S. White, E. D. Glowacki, T. Sekitani, T. Someya, N. S. Sariciftci, S. Bauer, *Nat. Commun.* **2012**, *3*; b) A. Facchetti, *Materials Today* **2013**, *16*, 123.
- [3] a) M. Campoy-Quiles, T. Ferenczi, T. Agostinelli, P. G. Etchegoin, Y. Kim, T. D. Anthopoulos, P. N. Stavrinou, D. D. C. Bradley, J. Nelson, *Nature Mater.* **2008**, *7*, 158; b) H. Sirringhaus, R. J. Wilson, R. H. Friend, M. Inbasekaran, W. Wu, E. P. Woo, M. Grell, D. D. C. Bradley, *Appl. Phys. Lett.* **2000**, *77*, 406.
- [4] a) J. Clark, C. Silva, R. H. Friend, F. C. Spano, *Phys. Rev. Lett.* **2007**, *98*, 206406; b) J. Piris, T. E. Dykstra, A. A. Bakulin, P. H. M. van Loosdrecht, W. Knulst, M. T. Trinh, J. M. Schins, L. D. A. Siebbeles, *J. Phys. Chem. C* **2009**, *113*, 14500; c) G. Grancini, M. Maiuri, D. Fazzi, A. Petrozza, H. J. Egelhaaf, D. Brida, G. Cerullo, G. Lanzani, *Nat. Mater.* **2013**, *12*, 29.
- [5] a) R. Noriega, J. Rivnay, K. Vandewal, F. P. V. Koch, N. Stingelin, P. Smith, M. F. Toney, A. Salleo, *Nat. Mater.* **2013**, *12*, 1037.
- [6] X. Li, W. C. H. Choy, L. Huo, F. Xie, W. E. I. Sha, B. Ding, X. Guo, Y. Li, J. Hou, J. You, Y. Yang, *Adv. Mater.* **2012**, *24*, 3046.
- [7] A. Hayakawa, O. Yoshikawa, T. Fujieda, K. Uehara, S. Yoshikawa, *Appl. Phys. Lett.* **2007**, *90*.
- [8] Z. He, C. Zhong, S. Su, M. Xu, H. Wu, Y. Cao, *Nat. Photonics* **2012**, *6*, 591.
- [9] R. F. Service, *Science* **2011**, *332*, 293.
- [10] H. Feng, Y. Luping, *J. Phys. Chem. Lett.* **2011**, *2*, 3102.
- [11] a) R. C. Coffin, J. Peet, J. Rogers, G. C. Bazan, *Nat. Chem.* **2009**, *1*, 657; b) O. P. Lee, A. T. Yiu, P. M. Beaujuge, C. H. Woo, T. W. Holcombe, J. E. Millstone, J. D. Douglas, M. S. Chen, J. M. J. Fréchet, *Adv. Mater.* **2011**, *23*, 5359; c) Y. M. Sun, G. C. Welch, W. L. Leong, C. J. Takacs, G. C. Bazan, A. J. Heeger, *Nat. Mater.* **2012**, *11*, 44.
- [12] a) A. K. K. Kyaw, D. H. Wang, D. Wynands, J. Zhang, T. Q. Nguyen, G. C. Bazan, A. J. Heeger, *Nano Lett.* **2013**, *13*, 3796; b) Y. Liu, C.-C. Chen, Z. Hong, J. Gao, Y. Yang, H. Zhou, L. Dou, G. Li, *Sci. Rep.* **2013**, *3*.
- [13] Mitsubishi Chemicals.
- [14] a) V. Coropceanu, J. Cornil, D. A. da Silva Filho, Y. Olivier, R. Silbey, J.-L. Bredas, *Chem. Rev.* **2007**, *107*, 926; b) D. Hertel, H. Baessler, *ChemPhysChem* **2008**, *9*, 666.
- [15] a) G. Grancini, D. Polli, D. Fazzi, J. Cabanillas-Gonzalez, G. Cerullo, G. Lanzani, *J. Phys. Chem. Lett.* **2011**, *2*, 1099; b) J.-L. Bredas, J. E. Norton, J. Cornil, V. Coropceanu, *Acc. Chem. Res.* **2009**, *42*, 1691; c) D. Moses, *Nat. Mater.* **2014**, *13*, 4; d) K. Vandewal, S. Albrecht, E. T. Hoke, K. R. Graham, J. Widmer, J. D. Douglas, M. Schubert, W. R. Mateker, J. T. Bloking, G. F. Burkhard, *Nat. Mater.* **2014**, *13*, 63.
- [16] a) J. Guo, H. Ohkita, H. Benten, S. Ito, *J. Am. Chem. Soc.* **2010**, *132*, 6154; b) H. Hoppe, N. S. Sariciftci, *J. Mater. Chem.* **2006**, *16*, 45; c) A. R. Campbell, J. M. Hodgkiss, S. Westenhoff, I. A. Howard, R. A. Marsh, C. R. McNeill, R. H. Friend, N. C. Greenham, *Nano Lett.* **2008**, *8*, 3942.
- [17] A. C. Morteani, R. H. Friend, C. Silva, *J. Chem. Phys.* **2005**, *122*.
- [18] J. R. Tumbleston, B. A. Collins, L. Yang, A. C. Stuart, E. Gann, W. Ma, W. You, H. Ade, *Nat. Photonics* **2014**, *8*, 385.
- [19] B. A. Collins, E. Gann, L. Guignard, X. He, C. R. McNeill, H. Ade, *J. Phys. Chem. Lett.* **2010**, *1*, 3160.
- [20] a) F. Dou, C. Silva, X. P. Zhang, *Chem. Phys. Lett.* **2013**, *572*, 44; b) J. S. Moon, C. J. Takacs, Y. Sun, A. J. Heeger, *Nano Lett.* **2011**, *11*, 1036.
- [21] a) H. Y. Wang, J. G. Liu, Y. Z. Xu, X. H. Yu, R. B. Xing, Y. C. Han, *Phys. Chem. Chem. Phys.* **2014**, *16*, 1441; b) J. S. Kim, W. S. Chung, K. Kim, D. Y. Kim, K. J. Paeng, S. M. Jo, S. Y. Jang, *Adv. Funct. Mater.* **2010**, *20*, 3538; c) W. C. Tsoi, W. M. Zhang, J. R. Hollis, M. Suh, M. Heeney, I. McCulloch, J. S. Kim, *Appl. Phys. Lett.* **2013**, *102*.
- [22] J. K. Lee, W. L. Ma, C. J. Brabec, J. Yuen, J. S. Moon, J. Y. Kim, K. Lee, G. C. Bazan, A. J. Heeger, *J. Am. Chem. Soc.* **2008**, *130*, 3619.
- [23] H. J. Fan, H. X. Shang, Y. F. Li, X. W. Zhan, *Appl. Phys. Lett.* **2010**, *97*.
- [24] a) A. Mishra, P. Bauerle, *Angew. Chem. Int. Ed.* **2012**, *51*, 2020; b) A. Tamayo, T. Kent, M. Tantitawat, M. A. Dante, J. Rogers, T. Q. Nguyen, *Energy Environ. Sci.* **2009**, *2*, 1180.
- [25] a) V. Palermo, P. Samori, *Angew. Chem. Int. Ed.* **2007**, *46*, 4428; b) J. Piris, M. G. Debije, N. Stutzmann, A. M. van de Craats, M. D. Watson, K. Mullen, J. M. Warman, *Adv. Mater.* **2003**, *15*, 1736.
- [26] S. D. Spencer, C. Bougher, P. J. Heaphy, V. M. Murcia, C. P. Gallivan, A. Monfette, J. D. Andersen, J. A. Cody, B. R. Conrad, C. J. Collison, *Sol. Energy Mater. Sol. Cells* **2013**, *112*, 202.
- [27] J. S. Zambounis, Z. Hao, A. Iqbal, *Nature* **1997**, *388*, 131.
- [28] K. Ichimura, K. Arimitsu, M. Tahara, *J. Mater. Chem.* **2004**, *14*, 1164.
- [29] a) E. D. Glowacki, M. Irimia-Vladu, M. Kaltenbrunner, J. Gasiorowski, M. S. White, U. Monkowius, G. Romanazzi, G. P. Suranna, P. Mastroianni, T. Sekitani, S. Bauer, T. Someya, L. Torsi, N. S. Sariciftci, *Adv. Mater.* **2013**, *25*, 1563; b) J. Lee, A. R. Han, J. Hong, J. H. Seo, J. H. Oh, C. Yang, *Adv. Funct. Mater.* **2012**, *22*, 4128; c) Y. Suna, J.-i. Nishida, Y. Fujisaki, Y. Yamashita, S. Aramaki, Y. Sakai, *Jpn. J. Appl. Phys.* **2008**, *47*, 4728.
- [30] A. B. Tamayo, B. Walker, T.-Q. Nguyen, *J. Phys. Chem. C* **2008**, *112*, 11545.
- [31] a) C. Kim, J. H. Liu, J. S. Lin, A. B. Tamayo, B. Walker, G. Wu, T. Q. Nguyen, *Chem. Mater.* **2012**, *24*, 1699; b) A. B. Tamayo, X. D. Dang, B. Walker, J. Seo, T. Kent, T. Q. Nguyen, *Appl. Phys. Lett.* **2009**, *94*.
- [32] a) E. J. MacLean, M. Tremayne, B. M. Kariuki, K. D. M. Harris, A. F. M. Iqbal, Z. M. Hao, *Perkin Trans.* **2000**, *1513*; b) S. T. Salmamal, J.-Y. Balandier, J.-B. Arlin, Y. Olivier, V. Lemaur, L. Wang, D. Beljonne, J. Cornil, A. R. Kennedy, Y. H. Geerts, B. Chattopadhyay, *J. Phys. Chem. C* **2013**, *118*, 657.
- [33] a) S. Y. Qu, H. Tian, *Chem. Commun.* **2012**, *48*, 3039; b) E. Ripaud, D. Demeter, T. Rousseau, E. Boucard-Cetol, M. Allain, R. Po, P. Leriche, J. Roncali, *Dyes Pigments* **2012**, *95*, 126; c) S. Stas, J.-Y. Balandier, V. Lemaur, O. Fenwick, G. Tregnago, F. Quist, F. Cacialli, J. Cornil, Y. H. Geerts, *Dyes Pigments* **2013**, *97*, 198.
- [34] E. D. Glowacki, G. Voss, K. Demirak, M. Havlicek, N. Sunger, A. C. Okur, U. Monkowius, J. Gasiorowski, L. Leonat, N. S. Sariciftci, *Chem. Commun.* **2013**, *49*, 6063.
- [35] J. Lakowicz, *Principles of Fluorescence Spectroscopy*, Springer, Berlin **2006**.
- [36] S. Frebort, Z. Elias, A. Lycka, S. Lunak, Jr., J. Vynuchal, L. Kubac, R. Hrdina, L. Burgert, *Tetrahedron Lett.* **2011**, *52*, 5769.
- [37] Z. Hao, O. Wallquist, *Europe Patent EP0763572 A2*, **1997**.